Journal of Power Sources 185 (2008) 1563–1568

Contents lists available at ScienceDirect

Journal of Power Sources

journal homepage: www.elsevier.com/locate/jpowsour

Hierarchical porous nickel oxide and carbon as electrode materials for asymmetric supercapacitor

Da-Wei Wang, Feng Li, Hui-Ming Cheng*

Shenyang National Laboratory for Materials Science, Institute of Metal Research, Chinese Academy of Sciences, 72 Wenhua Road, Shenyang 110016, PR China

ARTICLE INFO

Article history:
Received 4 June 2008
Received in revised form 7 August 2008
Accepted 18 August 2008
Available online 22 August 2008

Keywords:
Hierarchical pores
Nickel oxide
Carbon
Supercapacitor

ABSTRACT

Asymmetric supercapacitor is constructed using hierarchical porous electrode materials of nickel oxide and carbon with the aim to facilitate ion transport. Hierarchical porous nickel oxide and carbon are prepared by template-directed synthesis. Cyclic voltammetry (CV), electrochemical impedance spectroscopy (EIS) and galvanostatic charging–discharging are used to test the asymmetric supercapacitor and investigate the electrode processes at different supercapacitor voltages. The capacitance, energy density and power density of the asymmetric supercapacitor can be improved by elevating the supercapacitor voltage, and its cycling stability decays at high voltage, but the columbic efficiency stays close to 100%.

1. Introduction

Porous inorganic materials attract considerable interest and have made a great impact in many applications, including energy storage, catalysis and separation [1–6]. Many efforts have been devoted to the synthesis, characterization and applications of uniform mesoporous materials over the last decade, due to their attractive textural and structural features, e.g. highly ordered structures, ultrahigh surface area and narrow pore size distributions in the mesopore range, tuneable pore size and pore structure [1–5]. Progress has been made in structural, compositional and morphological control of mesoporous materials for their emerging applications [1–5]. However, practical applications require porous materials having pore structures at different size scales in order to achieve better performance [1,6]. Inclusion of macropores, mesopores and micropores in materials combines benefits from pores in different dimensional regimes. Hierarchical porous materials, which contain interconnected macro/meso/micropores, have enhanced performance for catalysis, separation and energy storage due to the increased mass transport through macropores and mesopores and maintenance of a specific surface area on the level of micropore systems [1,6].

Supercapacitors have been extensively investigated for decades due to the exponential growth of demand for portable electric devices and hybrid electric vehicles [7–9]. They serve as a backup energy device to batteries due to their higher power density. Two energy storage modes are applicable for supercapacitor: non-Faradaic electric double layer and Faradaic surface redox reaction. For electric double layer, the electric energy is stored in aggregated charges at the surface of electrode materials; and hence, porous carbons with large specific surface area are highly recommended. For redox reaction, the electric energy is usually generated by pseudocapacitive electron transfer between electrode and electrolyte. Metal oxides (RuO_2, NiO, etc.), functional groups and conductive polymers are all candidates for surface redox reactions. Asymmetric supercapacitors combining electric double layer anode and redox reaction cathode show promising capability to enhance the energy density due to higher capacitance and operation voltage while keeping excellent power density [10–17]. Unfortunately, the less-satisfied porous structures of electrode materials prevent improvement of asymmetric supercapacitors due to the poor ion transport which kinetically controls the electrochemical processes of charge storage and delivery.

As a consequence, hierarchical porous carbon anode and metal oxide cathode are promising for asymmetric supercapacitor with both high energy density and high power density. In this study, we prepared hierarchical porous nickel oxide and carbon by utilizing template-directed methods. Characterizations

* Corresponding author. Fax: +86 24 2390 3126.
E-mail address: cheng@imr.ac.cn (H.-M. Cheng).

0378-7753/$ – see front matter © 2008 Elsevier B.V. All rights reserved.
doi:10.1016/j.jpowsour.2008.08.032

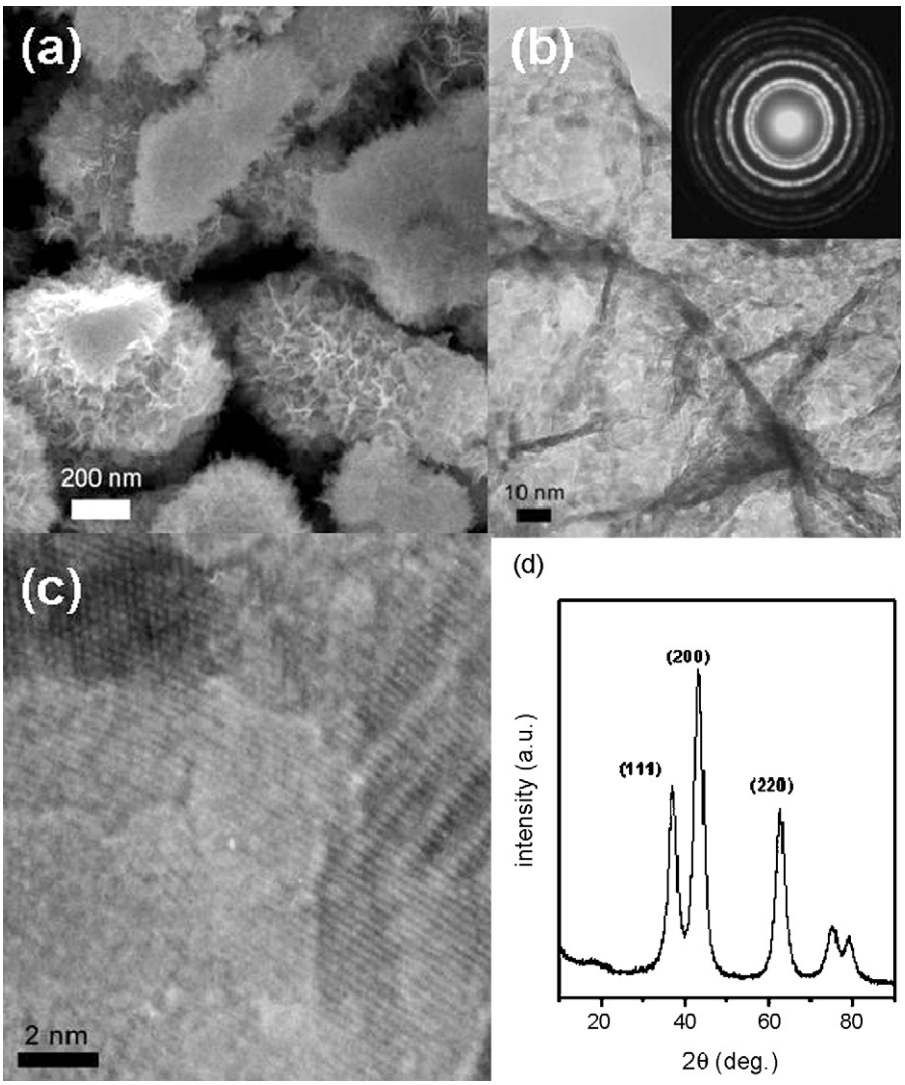

Fig. 1. (a) SEM image, (b) TEM image (inset is SAED pattern), (c) high-resolution TEM image and (d) X-ray diffraction profile of the nickel oxide electrode material.

using electron microscopy and nitrogen cryo-sorption techniques revealed the hierarchical porous texture of the products. Electrochemical performance of the asymmetric supercapacitor was evaluated.

2. Experimental

2.1. Preparation and characterization

Hierarchical porous nickel oxide was synthesized as follows: nickel nitrate (AR grade, Shenyang Chemicals, China), block copolymer P123 ($EO_{20}PO_{70}EO_{20}$, Aldrich), urea (AR grade, Shenyang Chemicals, China) and deionized water were taken in the mass of 20, 6.4, 50, and 200 g, respectively. This mixture was stirred at 26 °C to obtain a transparent solution, which was transferred to an autoclave and kept at 100 °C for 24 h. The precipitant was filtered, washed and dried at 80 °C for 12 h. The resulting material was then calcined in air at 300 °C for 3 h.

Synthesis of hierarchical porous carbon started with dropping typically 25 g of 20 wt% nickel nitrate solution into 50 g of 10 wt% sodium hydroxide solution while stirring. Subsequently, 25 g of 20 wt% ethanol solution of phenolic resin was added. The hybrid system was dried at 60 °C for 24 h and then carbonized in argon at 600 °C for 4 h. After carbonization, the inorganic species were etched with 3 M HCl solution. Thereafter the carbon product was obtained.

The samples were characterized by transmission electron microscope (TEM, JEOL JEM-2010, 200 kV) and scanning electron microscope (SEM, LEO SUPRA35, 15 kV). X-ray diffraction (XRD) patterns were collected using an RINT2200 (Cu Kα, λ = 1.5406 Å) at a step scan rate of 0.04°. Micro-Raman spectroscopy was performed using Jobin Yvon LabRam HR800, excited by 632.8 nm laser. Nitrogen cryo-sorption was measured on Micromeritics ASAP2010M.

2.2. Electrochemical measurements

Commercial nickel oxide was purchased (AR grade, Shenyang Chemicals, China) for a comparative study of the electrochemical performance of hierarchical porous nickel oxide. The working electrodes were prepared by mixing 90 wt% active material (carbon or nickel oxide), 5 wt% acetylene black, and 5 wt% polytetrafluoroethylene with ethanol to form slurries, and spreading onto a nickel-foam (1 cm^2). The mass load of active material on each electrode was 5 mg cm^{-2}. The electrochemical behavior of carbon and nickel oxide electrodes were firstly studied using a three-electrode cell with Ni foam as counter electrode and Hg/HgO

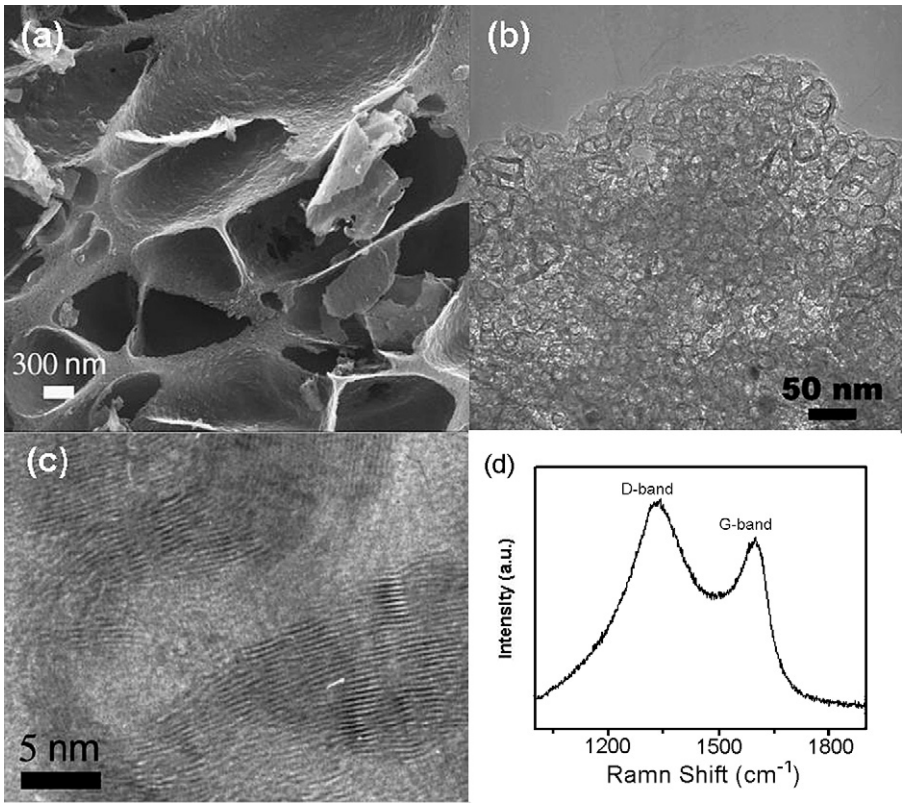

Fig. 2. (a) SEM image, (b) TEM image, (c) high-resolution TEM image and (d) Raman spectrum of the carbon electrode material.

as reference electrode. The asymmetric supercapacitor was then assembled in a sandwich-type two-electrode cell using carbon anode and nickel oxide cathode separated by a nylon paper. The electrolyte was 6 M KOH aqueous solution. The electrochemical performance was characterized by cyclic voltammetry (CV) and electrochemical impedance spectroscopy (EIS). The data was acquired using Solartron 1287/1260 electrochemical system. The cycling performance of asymmetric supercapacitor was examined on Arbin BT2000 at a current density of 1 A g^{-1} for 1000 cycles.

3. Results and discussion

A block-copolymer directed method was used to synthesize porous nickel hydroxide, by sintering which hierarchical porous nickel oxide was obtained. As shown by the SEM image in Fig. 1a, the nickel oxide has a flower-like macroporous morphology characterized by randomly agglomerated leaf-like units. Low magnification TEM image given in Fig. 1b reveals that the worm-like mesoporous texture of the leaf-like units, demonstrating a hierarchical porous feature. The selected-area electron diffraction (SAED) pattern given

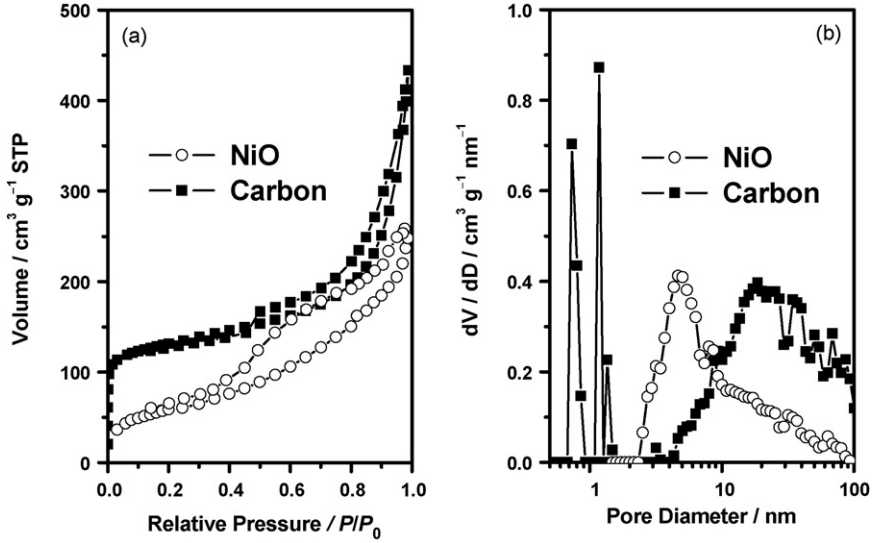

Fig. 3. (a) Nitrogen adsorption/desorption isotherms and (b) pore diameter distributions of the nickel oxide and carbon electrode materials.

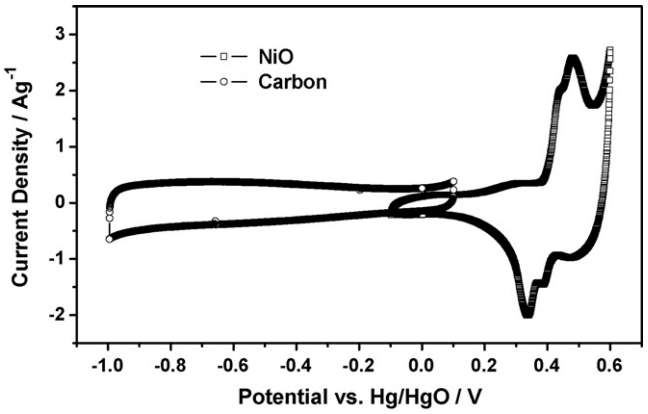

Fig. 4. Cyclic voltammetry profiles for the carbon and nickel oxide electrodes recorded at 2 mV s^{-1} in a three-electrode cell with Hg/HgO reference electrode and 6 M KOH electrolyte.

in inset is multi-crystalline. The worm-like mesopores are 3–6 nm in diameter and surrounded by nickel oxide nanocrystals, as is evident by high resolution TEM image in Fig. 1c. The lattice fringes of nickel oxide nanocrystals are recognizable with a *d* spacing of 2.5 Å for the (1 1 1) plane of rock salt type nickel oxide. Such an open hierarchical porous texture of nickel oxide permits easy access for ions to the electrode/electrolyte interface, which is crucial for surface Faradaic reactions [18–22]. The XRD profile of nickel oxide is illustrated in Fig. 1d. All the diffraction peaks can be assigned to rock salt nickel oxide. The electrochemical surface reactivity of nickel oxide is sensitively dependent on its crystallinity, which is related to the calcination temperature [18,19,23]. Many works demonstrated the highest capacitance of nickel oxide calcined at 300 °C [18,19,23,24].

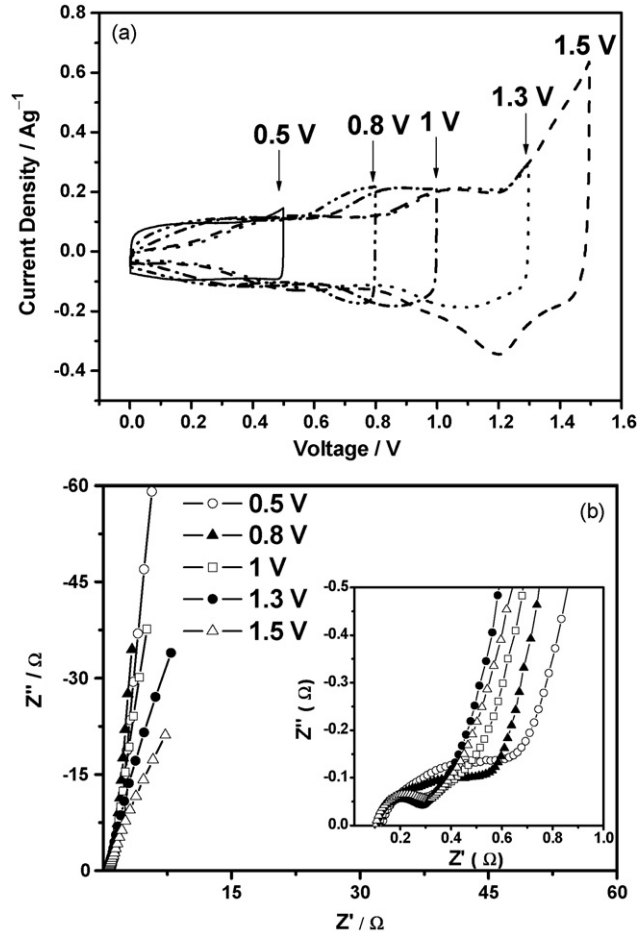

Fig. 5. (a) Cyclic voltammograms of the nickel oxide/carbon asymmetric supercapacitor with different operation voltage windows recorded at 2 mV s^{-1}; (b) electrochemical impedance spectra of the asymmetric supercapacitor at different voltages. Data was obtained with a two-electrode sandwich-type cell in 6 M KOH electrolyte.

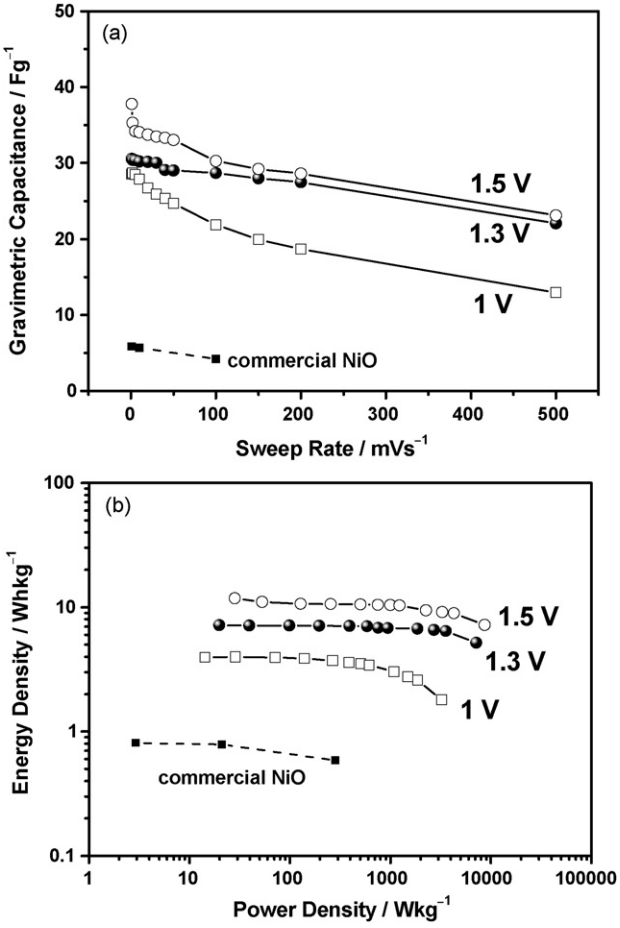

Fig. 6. (a) Gravimetric capacitance dependence on sweep rates and (b) Ragone plots for the asymmetric supercapacitor operated at different voltages. The device with commercial NiO as positive electrode was compared.

An inorganic template technique was utilized to fabricate hierarchical porous carbon. SEM image in Fig. 2a shows the macroporous texture of carbon electrode material. The macroporous cores exhibit a foam-like morphology surrounded by thin walls with thickness of hundred nanometers. TEM image in Fig. 2b reveals the mesoporous texture of the walls. The mesopores are 4–50 nm in diameter. These mesopores can provide short and low-resistant ion transport paths throughout the walls approaching to micropores, which are essential sites for electric double layer charge storage. Most importantly, the mesoporous walls possess localized graphitic structure giving an enhanced electric conductivity, which is important for electron transfer during electrochemical processes (Fig. 2c). Raman spectrum in Fig. 2d shows the weak intensity of G-band indicating the lower fraction of localized graphitic carbon than amorphous carbon in the sample.

The SEM and TEM observations clearly demonstrate the hierarchical porous texture of nickel oxide and carbon electrode materials. Nitrogen cryo-sorption technique was utilized to confirm the hierarchical porous characteristics of the materials. The

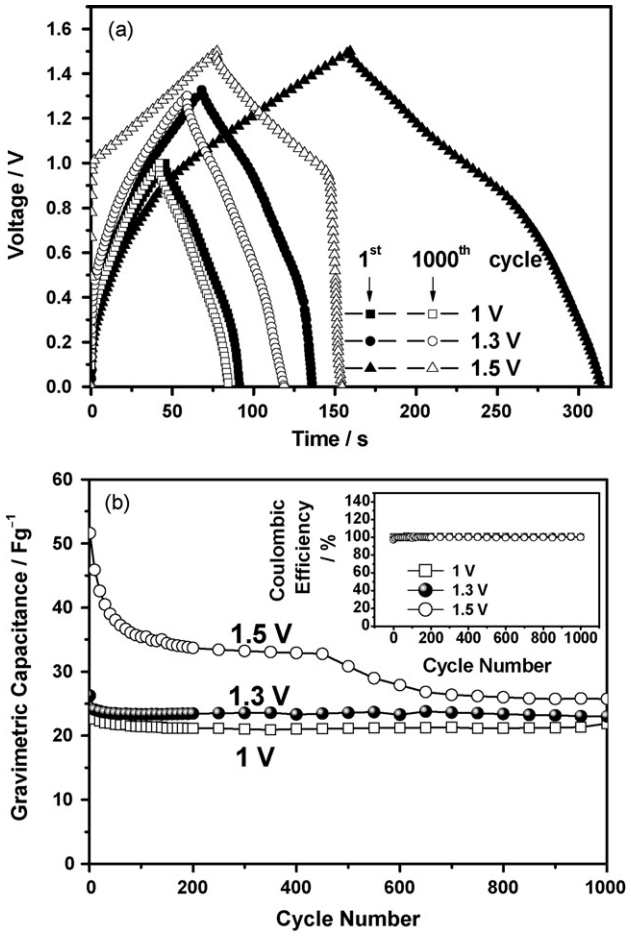

Fig. 7. (a) Galvanostatic charging/discharging curves at 1st and 1000th cycles and (b) cycling stability (inset is columbic efficiency) for the asymmetric supercapacitor operated at different voltages.

nitrogen adsorption–desorption isotherms at 77 K and pore diameter distributions of nickel oxide and carbon are presented in Fig. 3. Considering the negligible amount of nitrogen adsorption at low relative pressure, it can be concluded that the micropore contribution to the total pore volume was low for nickel oxide. As shown in Fig. 3a, the adsorption curve gradually increases in the middle-pressure region ($\sim 0.4P/P_0$) and then climbs abruptly in the high-pressure region ($>0.7P/P_0$). The Brunauer–Emmett–Teller (BET) surface area, total pore volume and average pore diameter of nickel oxide are 220 $m^2\ g^{-1}$, 0.37 $cm^3\ g^{-1}$ and 6.7 nm. The pore diameter distribution in Fig. 3b shows the abundance of mesopores between 2 and 10 nm. The shoulder on the larger pore side indicates existence of larger mesopores and macropores. Nitrogen isotherm of carbon exhibits the combined characteristics of type-I/II, with a BET surface area of 460 $m^2\ g^{-1}$, total pore volume of 0.57 $cm^3\ g^{-1}$, and average pore diameter of 5.1 nm. Three regions can be identified in the pore diameter distribution curve: (1) ultrafine micropores (<1 nm) and micropores (1–2 nm), (2) mesopores (4–50 nm), and (3) macropores (60–100 nm). These results confirm the hierarchical porous texture of nickel oxide and carbon electrode material.

The different electrochemical behaviors of carbon and nickel oxide electrodes were measured using cyclic voltammetry at 2 mV s^{-1} in a three-electrode cell with 6 M KOH electrolyte and Hg/HgO reference electrode, as illustrated in Fig. 4. The CV curve for carbon electrode is representative of electric double layer charging/discharging. However, the CV result of nickel oxide electrode is distinct and more complicated. When the electrode potential is smaller than 0.2 V versus Hg/HgO, surface charge storage mainly comes from electric double layer charging–discharging. Polarizing the electrode to more positive potential initiates the multiple redox reactions with cathodic peaks at 0.43 and 0.48 V and anodic peaks at 0.39 and 0.33 V versus Hg/HgO. Thermal gravimetric analysis of nickel oxide revealed weight loss relative to the decomposition of untransformed nickel hydroxide species (not shown). It is reasonable to have nickel hydroxide residue due to the relatively low calcination temperature of 300 °C [22]. Therefore, this complex CV behavior can be attributed to the redox reactions related to NiO/NiOOH and $Ni(OH)_2$/NiOOH [22]. The sharp peak at 0.6 V versus Hg/HgO comes from the decomposition of water on the surfaces of nickel oxide electrode.

Carbon anode and nickel oxide cathode were used to construct an asymmetric supercapacitor. Cyclic voltammetry was used to evaluate the applicable operation voltage window (OVW) of the asymmetric supercapacitor at low sweep rate of 2 mV s^{-1}, as shown in Fig. 5a. When the OVW is 0.5 V, only charge propagation in the electric double layer is observed. By increasing the OVW to 0.8 V, oxidation and reduction humps appear in the charging–discharging branch, implying the beginning of Faradaic redox reactions on nickel oxide electrode. Further increasing the OVW to 1.0 V, the redox humps show the pseudo-capacitive properties. When the OVW is raised to 1.3 and 1.5 V, significant increments in the positive current are noticed, indicating the more severe redox reactions on the surface of nickel oxide electrode. Electrochemical impedance spectra explored at different OVW are shown in Fig. 5b. The spectra recorded at 0.5 and 0.8 V show vertical lines at low frequency which are characteristic of supercapacitive behavior, and the inclined

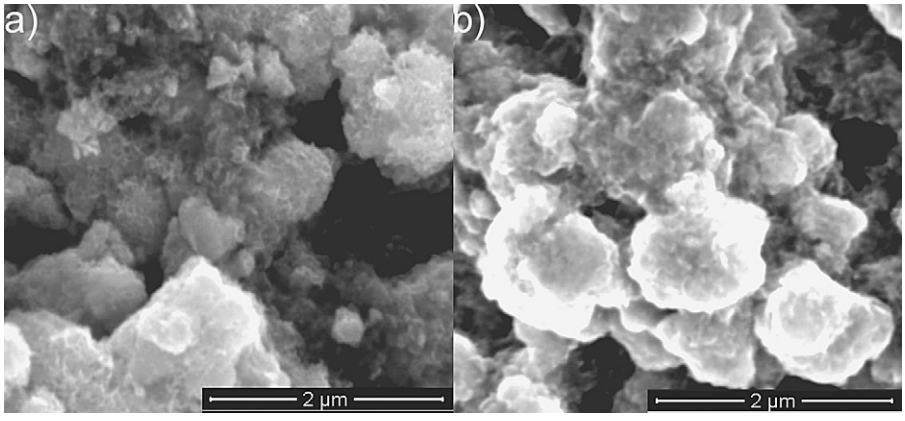

Fig. 8. Surface morphology evolution of nickel oxide cathode: (a) before cycle and (b) after 1000 cycles operated at 1.5 V.

Warburg-like curves at high frequency indicate a typical electric double layer behavior. Spectra measured at 1, 1.3 and 1.5 V also exhibit nearly vertical lines. However, the more inclined features for spectra recorded at 1.3 and 1.5 V show the effect of high operation voltages on supercapacitive behavior due to the more pronounced surface redox reactions. The apparent semicircles at high frequency also represent the occurrence of surface redox Faradaic reactions on nickel oxide cathode.

We demonstrate the capacitance rate performance of the asymmetric supercapacitor at different OVW in Fig. 6a. The capacitance was calculated using the total mass of active materials on the two electrodes in the asymmetric supercapacitor, rather than single electrode. Disregarding the OVW applied, the highest capacitance is obtained at 1 mV s^{-1}, and the lowest capacitance at 500 mV s^{-1}. At 1.0 V OVW, the highest capacitance is 28 F g^{-1}, while the lowest value is only 13 F g^{-1} with a 50% decayed ratio. For OVW of 1.3 V, the highest capacitance is 30 F g^{-1}, and the lowest value is 22 F g^{-1} with a 33% decayed ratio. For OVW of 1.5 V, the highest capacitance is 37 F g^{-1}, and the lowest value is 23 F g^{-1}, with a 38% decayed ratio. The higher gravimetric capacitance at higher OVW is attributed to the redox reactions. It is worth mentioning that the best rate capacitance performance is obtained at 1.3 V. In addition, because of the high OVW and capacitance, much improved power density and energy density can be realized. Fig. 6b gives the power density and energy density of the asymmetric supercapacitor operated at 1.0, 1.3 and 1.5 V. It is obvious that both the power density and energy density are significantly enhanced upon raising the operation voltage. The strengthened energy densities at 1.3 V and 1.5 V are ascribed to the high voltages and the increased capacitance due to Faradaic reactions. Power density is the deliverable energy density per unit time, and as evidenced in Fig. 6b, the power density also increases as the supercapacitor voltage increases. To clarify the advantages of hierarchical porous nickel oxide as cathode materials for asymmetric supercapacitor, we further studied the performance of commercial nickel oxide, as displayed in Fig. 6a and b. It is clear that the capacitance retention ratio at 100 mV s^{-1} for commercial nickel oxide is 72%, smaller than 76% for the hierarchical porous nickel oxide. Importantly, the capacitance, power density and energy density performance of commercial nickel oxide are far poor than that obtained for hierarchical porous nickel oxide. These results highlight that both the high specific surface area and hierarchical porous texture are crucial for developing asymmetric supercapacitors with excellent power and energy performance.

Galvanostatic charging–discharging behaviors at the 1st and 1000th cycles of the asymmetric supercapacitor are demonstrated in Fig. 7a. It is obvious that the voltage–time profiles retain the original shapes for the supercapacitor operated at 1.0 and 1.3 V. However, the voltage–time profile for the supercapacitor operated at 1.5 V changes greatly after 1000 cycles, indicating the significant deterioration of the electrode reactivity. As analyzed using CV and EIS, this result can be attributed to the severe redox reactions occurred on the electrode surfaces at high voltage, which probably resulted in deformation of electrode nickel oxide active materials. To confirm this point, we characterized the nickel oxide cathode after operating at 1.5 V for 1000 cycles using SEM, as shown in Fig. 8. It was found that the hierarchical porous texture changed from rough exterior surfaces to relatively smooth morphology after the repeated long redox reaction. This resulted in the loss of electrochemical reactive surfaces and hence the decayed performance. As shown in Fig. 7b. it is obvious that the cycling stability of asymmetric supercapacitors operated at 1.0 and 1.3 V is superior to that operated at 1.5 V. The capacitance measured at 1.5 V in the first cycle exceeds 50 F g^{-1}. However, this value is sharply decreased to 35 F g^{-1} after 100 cycles, and finally stays at 25 F g^{-1} after 1000 cycles. The inferior cycling stability at 1.5 V arises from the electrolyte decomposition, which decreases active sites on the electrode surfaces. The columbic efficiency given in inset of Fig. 7b stably stays at about 100%, independent of the voltage applied.

4. Conclusions

An asymmetric supercapacitor was assembled with hierarchical porous nickel oxide as cathode material and carbon as anode material, which were synthesized by template-directed methods. By increasing the supercapacitor voltage, the device capacitance can be increased significantly from 28 F g^{-1} at 1.0 V to 38 F g^{-1} at 1.5 V. The capacitance increment was attributed to the Faradaic charge conversion associated with nickel oxide cathode at high voltages. Considering the combined performance of energy-power densities and cycling stability, the best operation voltage window of this asymmetric supercapacitor was 1.3 V.

Acknowledgement

We acknowledge the financial support from the NSFC of PR China (no. 50632040).

References

[1] Z.Y. Yuan, B.L. Su, J. Mater. Chem. 16 (2006) 663–667.
[2] J. Lee, J. Kim, T. Hyeon, Adv. Mater. 18 (2006) 2073–2094.
[3] A.H. Lu, F. Schuth, Adv. Mater. 18 (2006) 1793–1805.
[4] Y.Q. Wang, C.M. Yang, W. Schmidt, B. Spliethoff, E. Bill, F. Schuth, Adv. Mater. 17 (2005) 53–56.
[5] X.Y. Lai, X.T. Li, W.C. Geng, J.C. Tu, J.X. Li, S.L. Qiu, Angew. Chem. Int. Ed. 46 (2007) 738–741.
[6] D.W. Wang, F. Li, M. Liu, G.Q. Lu, H.M. Cheng, Angew. Chem. Int. Ed. 47 (2008) 373–376.
[7] B.E. Conway, Electrochemical Supercapacitors: Scientific Fundamentals and Technological Applications, Kluwer Academic/Plenum, New York, 1999, pp. 11–15.
[8] R. Kötz, M. Carlen, Electrochim. Acta 45 (2000) 2483–2498.
[9] E. Frackowiak, F. Béguin, Carbon 39 (2001) 937–950.
[10] H. Inoue, T. Morimoto, S. Nohara, Electrochem, Solid State Lett. 10 (2007) A261–A263.
[11] S.B. Ma, K.W. Nam, W.S. Yoon, X.Q. Yang, K.Y. Ahn, K.H. Oh, K.B. Kim, Electrochem. Commun. 9 (2007) 2807–2811.
[12] T. Brousse, P.L. Taberna, O. Crosnier, R. Dugas, P. Guillemet, Y. Scudeller, Y. Zhou, F. Favier, D. Belanger, P. Simon, J. Power Sources 173 (2007) 633–641.
[13] V. Ganesh, S. Pitchumani, V. Lakshminarayanan, J. Power Sources 158 (2006) 1523–1532.
[14] V. Khomenko, E. Raymundo-Pinero, F. Beguin, J. Power Sources 153 (2006) 183–190.
[15] Y.G. Wang, L. Cheng, Y.Y. Xia, J. Power Sources 153 (2006) 191–196.
[16] Y.G. Wang, L. Yu, Y.Y. Xia, J. Electrochem. Soc. 153 (2006) A743–A748.
[17] C.Z. Yuan, X.G. Zhang, Q.F. Wu, B. Gao, Solid State Ion. 177 (2006) 1237–1242.
[18] W. Xing, F. Li, Z.F. Yan, G.Q. Lu, J. Power Sources 134 (2004) 324–330.
[19] M.Q. Wu, J.H. Gao, S.R. Zhang, A. Chen, J. Porous Mater. 13 (2006) 407–412.
[20] D.D. Zhao, M.W. Xu, W.H. Zhou, J. Zhang, H.L. Li, Electrochim. Acta 53 (2008) 2699–2705.
[21] W.J. Zhou, J. Zhang, T. Xue, D.D. Zhao, H.L. Li, J. Mater. Chem. 18 (2008) 905–910.
[22] M.W. Xu, S.J. Bao, H.L. Li, J. Solid State Electrochem. 11 (2007) 372–377.
[23] K.W. Nam, W.S. Yoon, K.B. Kim, Electrochim. Acta 47 (2002) 3201–3209.
[24] K.W. Nam, K.B. Kim, J. Electrochem. Soc. 149 (2002) A346–A354.